Hindawi
International Journal of Photoenergy
Volume 2023, Article ID 4225831, 21 pages
https://doi.org/10.1155/2023/4225831

Research Article

A New High-Performance Photovoltaic Emulator Suitable for Simulating and Validating Maximum Power Point Tracking Controllers

Ambe Harrison [1] **and Njimboh Henry Alombah** [2]

[1]*Department of Electrical and Electronics Engineering, College of Technology (COT), University of Buea, P.O. Box 63, Buea, Cameroon*
[2]*Department of Electrical and Electronics Engineering, College of Technology, University of Bamenda, P.O. Box 39, Bambili, Cameroon*

Correspondence should be addressed to Ambe Harrison; ambe.harrison@ubuea.cm

Received 22 February 2023; Revised 23 March 2023; Accepted 5 April 2023; Published 20 April 2023

Academic Editor: Fayaz Hussain

Copyright © 2023 Ambe Harrison and Njimboh Henry Alombah. This is an open access article distributed under the Creative Commons Attribution License, which permits unrestricted use, distribution, and reproduction in any medium, provided the original work is properly cited.

Photovoltaic (PV) research is rapidly growing, and the need for controlled environments to validate new MPPT controllers is becoming increasingly important. Currently, researchers face several challenges in testing MPPT algorithms due to the unpredictable nature of solar PV power generation. In this paper, we propose a new photovoltaic emulator (PVE) that could replace solar panels and ensure a highly controllable environment suitable for testing photovoltaic (PV) systems. In this PVE, the complex nonlinear equations of the PV cell/module are fast computed and resolved by a new linearization technique which involves the systematic breakdown of the current-voltage (I-V) curve of the PV into twelve linear segments. Based on input environmental conditions, an artificial neural network (ANN) was constructed to assist the linearization process by predicting the current-voltage boundary coordinates of these segments. Using simple linear equations, with the segment boundary coordinates, a reference voltage was generated for the PVE. A nonlinear backstepping controller was designed to exploit the reference voltage and stabilize the power conversion stage (PCS). The PVE was optimized using particle swarm optimization (PSO). Several tests have shown that the proposed nonlinear controller provides better dynamic and robust performance than the PI controller, the most reputable and recurrent control method in the area of PVE. The PVE was coupled with a recently proposed integral backstepping MPPT controller and analyzed under several dynamic conditions, including the MPPT test specified by EN 50530. It was found that the accuracy of the proposed PVE measured by its relative error is less than 0.5%, with an MPPT efficiency of greater than 99.5%. The attractive results achieved by this PVE make it especially suitable for simulating and validating MPPT controllers.

1. Introduction

The last decade has seen tremendous attention given to renewable energies. There is no doubt that resorting to renewable energy sources is one of the most effective alternatives to accelerate the energy transition. Thus, renewable energy progress has been promising, with recent estimates from the International Energy Agency (IEA) suggesting that 2022 was a record year for renewable energy, with an estimated 340 GW of capacity. The IEA reports that even though renewable energy deployment is on the rise, its global contribution must grow faster by 2050 to achieve net zero emissions, where renewable energy generates more than 60% of electricity by 2030. Consequently, there has been a dramatic increase in the penetration of renewable energy sources (RSEs) into the grid [1, 2]. It has been shown that microgrids [3, 4] are a promising way to supply electrical power to isolated rural communities that are not accessible to main power grids [5] As solar PV power is integrated into the grid, it is necessary to consider topics such as

maximum power point tracking (MPPT), grid inverters, modulation and propagation of harmonic signals, and others [6]. Currently, there is a growing interest in using maximum power point tracking (MPPT) as a method of optimizing solar PV systems. As a result, several MPPT algorithms/controllers have been developed during the last year, and more are expected as PV system research continues to be stimulated. Therefore, as photovoltaic (PV) research grows, it becomes important to seek a controllable environment to properly simulate and validate new MPPT controllers. Currently, researchers are facing several problems in testing maximum power point-tracking algorithms and controllers. This is attributable to the fact that solar PV power generation depends on uncontrollable environmental conditions including irradiance and temperature. Therefore, the challenge in testing new MPPT controllers lies in ensuring that a controllable environment is available, which is often a daunting task. To address these problems, PV emulators have been proposed as a replacement for PV systems [7–10], allowing researchers to easily set up testing profiles.

The photovoltaic emulator (PVE) is a power electronic-based system that simulates the static and dynamic characteristics of solar cells in a wide range of conditions [8]. One of the most important subsystems of a PVE is the power conversion stage (PCS), which can either be linear [10] or nonlinear [11]. Although PVEs based on linear power supplies perform exceptionally well, their efficiency is seldom high, making them suitable only for low-power applications. In contrast, PVEs based on a nonlinear power supply provide better performance at higher efficiency and lower cost; hence, they are suitable for relatively higher power applications.

By employing a buck converter in the power conversion stage (PCS) and the PI controller in the control stage, Ref. [12] proposed a dynamic PVE emulator with attractive dynamic and static performances. Although their emulator showed attractive performances, its main flaw is the low-level control in the power stage, typically by the use of a PI controller. Although the PI controller provides a simple control solution, it requires linearization of the system under control over a small operating region. To generate similar features as an actual PV, the photovoltaic emulator (PVE) should operate over a broad spectrum. Therefore, linearizing the power conversion stage as performed in [12] makes the PVE functional within the small region from which the linearized models were obtained. Additionally, certain nonlinear and robust features necessary for a PVE are destroyed in the process of linearization. In addition to dynamic features, the PVE is supposed to be accurate. Therefore, the control stage is usually fed by a reference voltage or current signal. The researchers [12–14] resorted to the analytical and numerical methods for resolving the nonlinear complex mathematical equations of the PV cell/module to provide a reference signal to the PI controller. The accurate design of a PVE system based on analytical or numerical resolutions is difficult; in particular, the nonlinear current-voltage (I-V) curves of the PV demand significant computational effort and resources. One of the main challenges in the design of the PVE is the complex resolution of the nonlinear equations of the PV model [15].

The research work in [15] addressed the challenge of resolving the nonlinear equations of the PV by linearizing the I-V curve into four linear segments. Treating the I-V curve by linearization offers several benefits over the analytical or numerical approaches, principally because it is simple and demands lower computational efforts. Hence, the works of [15] encompass all these rich benefits. However, its main limitation lies in the weak accuracy achieved by considering just four linear segments in resolving the whole I-V curve. Additionally, the work was not extended to an MPPT context. Moreover, by employing a PI controller in their control loop [15], the PVE will exhibit similar limitations as was previously discussed. As could be seen in [15], the PVE demonstrated a weak dynamic response to changing load and irradiance, respectively.

By resorting to an instantaneous output impedance matching (IOIM) controller, Ref. [7] tackled the dynamical problems of the PVE. The IOIM is based on load resistance feedback which generates the PVE voltage reference signal and an inner boundary control (BC) scheme that regulates the converter at the given reference. The conventional PVE suffers from oscillation in one region of operation (i.e., in constant voltage region (CVR) with current-mode control and constant current region (CCR) with voltage-mode (VM) control) as the feedback signal always has an ac ripple [7]. The oscillation-based ripple problem in the PVE control was addressed in [7], by employing load resistance feedback in the reference voltage generation algorithm. Their works show attractive results, however limited by 2 facts; the control scheme is linear PI based, and secondly, the reference generation is inherently based on the lookup table which has a very limited range of operation. A similar resistance feedback PVE developed by [16] addressed the problem of control in the PVE, but the overlinearity of the system using the PI linear controller reduces the range of operation and sacrifices the dynamic robustness of the PVE.

In this paper, a new photovoltaic emulator (PVE) is proposed to emulate the full dynamic and static characteristics of the PV cell/module. To guarantee a broad spectrum of operation, as well as ensure the highly robust dynamic performance of the PVE, we resort to a nonlinear control strategy to stabilize the power conversion stage of the PVE. Furthermore, to consolidate simplicity in treating and resolving the nonlinear complex equations of the PV, we propose a new linearization that involves piecewise linearization of the I-V curve into 12 segments. The strength of the proposed PVE is confirmed by testing it with a nonlinear MPPT controller. The proposed PVE and its control strategy was found better than the PI controller, which is the most reputable control technique in the current literature of PVE. Furthermore, by resorting to a higher order segmentation approach, the proposed PVE archives higher accuracy than the four segment-based PVE approach in [15]. The excellent and promising results achieved by the proposed PVE show that it is very suitable for simulating and validating MPPT controllers. The rest of the paper is composed as follows. The model of the reference PV is presented in Section 2. In Section 3, the proposed PVE is designed and elaborated from a subsystem point of view. The proposed PVE-

coupled MPPT system is discussed in Section 4. The results of this paper are presented and discussed in Section 5, while a conclusion is provided in Section 6.

2. Modelling of the Reference PV Model

The equivalent circuit of the PV reference model is shown in Figure 1. It is based on the single diode which offers a good compromise between complexity and performance [17–20]. It consists mainly of a photocurrent source that responds to irradiance (G) through the flow of current I_{ph}, a diode D, carrying current I_{D}, the parallel and series resistors R_{p}, R_{s} carrying current I_{p} and I_{pv}, respectively. At the terminal of the cell, a voltage termed V_{pv} is available. The PV current governing the single diode can be written as

$$I_{\text{pv}} = N_{\text{p}} I_{\text{ph}} - N_{\text{p}} I_{\text{s}} \left[\exp\left(\frac{q\left(V_{\text{pv}} + \left(N_{\text{s}}/N_{\text{p}}\right) I R_{\text{s}}\right)}{N_{\text{s}} n k T} \right) - 1 \right] - \frac{V_{\text{pv}} + \left(N_{\text{s}}/N_{\text{p}}\right) I_{\text{pv}} R_{\text{s}}}{\left(N_{\text{s}}/N_{\text{p}}\right) R_{\text{p}}}. \tag{1}$$

A PV power system will often contain a large number of cells in series (N_{s}) and in parallel (N_{p}), to match a particular level of voltage/power rating. In Equation (1), q, n, k, T, and I_{s} are the charge constant, diode ideality factor, Boltzmann constant, cell operating temperature, and diode saturation current, respectively. From the same equation, the parameters I_{ph} and I_{s} are environmentally dependent in one way or the other. It is therefore convenient to write I_{ph} as $I_{\text{ph}}(G, T)$ and I_{s} as $I_{\text{s}}(T)$ to convey the sense of dependence on environmental conditions G and T. These parameters are defined as

$$I_{\text{ph}}(G, T) = \frac{G}{G_{\text{ref}}} \left(I_{\text{ph-ref}} + K_i (T - T_{\text{ref}}), \right. \tag{2}$$

$$I_{\text{s}}(T) = I_{\text{s-ref}} \left(\frac{T}{T_{\text{ref}}} \right)^3 \exp\left[\frac{q E_{\text{g}}}{n k} \left(\frac{1}{T_{\text{ref}}} - \frac{1}{k T} \right) \right]. \tag{3}$$

If $N_{\text{p}} = 1$, that is a single PV module, as is the case in this paper. Then, Equation (1) reduced to

$$I_{\text{pv}} = I_{\text{ph}} - I_{\text{s}} \left[\exp\left(\frac{q\left(V_{\text{pv}} + N_{\text{s}} I R_{\text{s}}\right)}{N_{\text{s}} n k T} \right) - 1 \right] - \frac{V_{\text{pv}} + N_{\text{s}} I_{\text{pv}} R_{\text{s}}}{N_{\text{s}} R_{\text{p}}}. \tag{4}$$

It can be inferred from Equations (2) and (3) that irradiance (G) and operating temperatures (T) are indispensable environmental parameters. The terms $I_{\text{s-ref}}$, E_{g}, $I_{\text{ph-ref}}$, and G_{ref} are the saturation current at the reference (standard test conditions (STC)), the energy gap in electron volts, the reference photocurrent, and the reference irradiance (1000 W/m^2). The term K_i is the temperature coefficient of current readily provided by the manufacturer. By inspection, we can see from Equation (4) that the relationship between the PV current and PV voltage is nonlinear. In this paper, we are going to resort to piecewise linearization to resolve this system of equations.

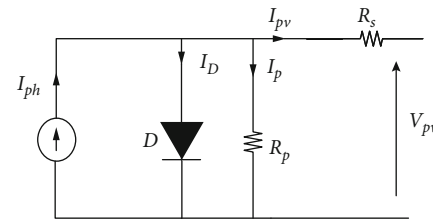

Figure 1: Single-diode equivalent circuit of the PV.

3. Design of the Proposed Photovoltaic Emulator

Synoptically, the proposed photovoltaic emulator (PVE) can be seen in Figure 2. It consists of an artificial neural network-(ANN-) based linear reference voltage generator, which provides a reference voltage, $x_{\text{r.pve}}$, to the close controlled system. The reference generator principally responds to the environmental inputs, temperature (T), and irradiance (G). Therefore, the operator can manually set the desired values or profiles of irradiance and temperature for his tests, hence making the overall system entirely controllable. A voltage comparator compares the error between $x_{\text{r.pve}}$ and the actual PVE output voltage, V_{pve}. The resulting error is fed to a nonlinear backstepping controller (BSC). Fed with feedback measurements of the inductor current (i_L) from the power conversion stage (PCS) and V_{pve}, the BSC ensures that the voltage error runs to zero. This is achieved by a nonlinear control law (u_{pve}). Hence, the stability and robustness of the entire PVE lie with the nonlinear. Therefore, from a synoptic point of view, the proposed PVE is made up of three main subsystems. In this section, we are going to proceed with the subsystem-by-subsystem design of the proposed PVE.

3.1. PVE Reference Voltage Generation. Given the nonlinear inherent nature of the PV as inferred from its electrical equation, it is a huge computational burden to directly solve its I-V curve. This is the limitation of most PVE. To get rid of this tremendous computational burden, we are proposing to piecewise linearize the entire I-V curve into 12 linear segments. By using the (voltage-current) boundary coordinates of these segments, the reference voltage for the PVE can be generated. To ensure a broad environmental spectrum, an ANN can be employed to assist the linearization scheme, by predicting the boundary coordinates of these segments.

As seen in Figure 3, we propose to break down the I-V curve into 12 linear segments. The boundary coordinates of these segments are labeled a to m. We chose to assign them the following coordinate variables $a(0, I_{\text{sc}})$, $b(I_1, V_1)$, $c(I_x, V_x)$, $d(I_2, V_2)$, $e(I_{xxx}, V_{xxx})$, $f(I_3, V_3)$, $g(I_{\text{mpp}}, V_{\text{mpp}})$, $h(I_4, V_4)$, $i(I_{xxxx}, V_{xxxx})$, $j(I_5, V_5)$, $k(I_{xx}, V_{xx})$, $l(I_6, V_6)$, $m(0, V_{\text{oc}})$. We note that these coordinates appear in pair of

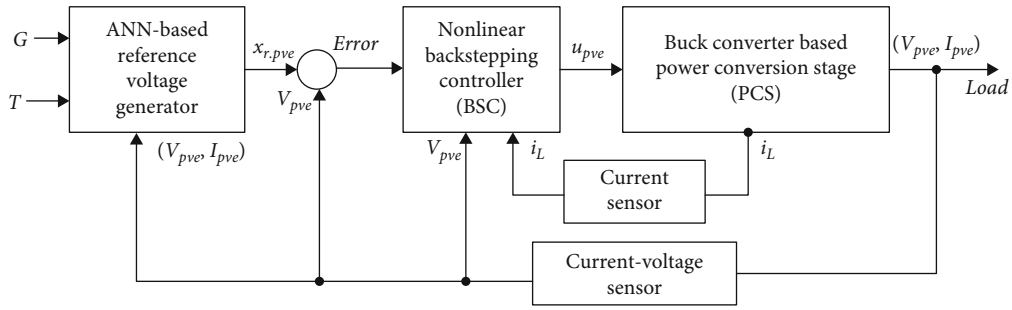

Figure 2: Closed loop controlled system of the proposed PVE.

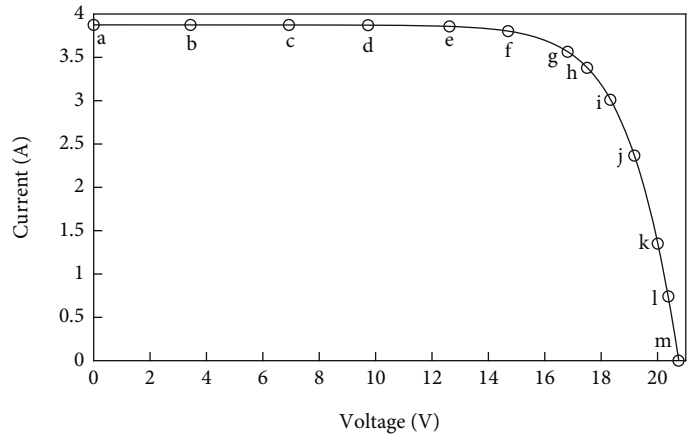

Figure 3: 12-segment-based linearization of the PV I-V curve.

current-voltage. This means that, from the I-V curve model, having the voltage value, we can directly infer its corresponding current pair.

It is imperative to precisely define the coordinates of these (a-m) segments. We are in a position to clearly label these points. The coordinates $a(0, I_{sc})$, $g(I_{\text{mpp}}, V_{\text{mpp}})$, $m(0, V_{\text{oc}})$ are obvious, since the short circuit current I_{sc}, maximum power point current, and voltage $I_{\text{mpp}}, V_{\text{mpp}}$ of the PV module can be known from the model if G and T are precisely available. We recall that when dealing with the coordinate (pair of current-voltage) if we have the voltage, the current can be easily extracted from the PV model. The voltage coordinate of segments $c(I_x, V_x)$, and $k(I_{xx}, V_{xx})$ is obtained as shown in Equation (A.1) of the appendix. Similarly, the voltage coordinate of the segments $e(I_{xxx}, V_{xxx})$ and (I_{xxxx}, V_{xxxx}) is presented in Equation (A.2) of the Appendix. The rest of the voltage boundary coordinates are obtained as shown in Equations (A.3)–(A.6) of the appendix.

According to the Sandia International Photovoltaic Modeling Laboratory [21], the voltage coordinate point V_x and V_{xx} can be obtained as $V_x = V_{\text{oc}}/2$ and $V_{xx} = (V_{\text{oc}} + V_{\text{mpp}})/2$. In the proposed 12-segment linearization method, we desire that V_x be closer to the short-circuit point (a) and V_{xx} closer to the open-circuit point. Hence, rather than taking a division by a factor of 2 in either case, we divide by 2.44 and 1.88, respectively, as inferred from Equation (A.1) of the appendix. A similar analogy is applied to the voltage coordinates of e and i. We seek good coverage of the I-V curve; therefore, we desire that the voltage coordinate of $e(V_{xxx})$ and $i(V_{xxxx})$ be closer to the maximum power point (g). To achieve this, there is a division by the factor of 1.88 for $e(V_{xxx})$ and by 2.44 for $i(V_{xxxx})$, as inferred from Equation (A.2) of the appendix. By looking at the boundary voltage coordinate that contains the V_i's that is V_1 to V_6, we notice that V_i is closely bounded by two other boundary voltage coordinates. For example $b(I_1, V_1)$ is bounded by $a(0, I_{\text{sc}})$ and $c(I_x, V_x)$ and $l(I_6, V_6)$ bounded by $k(I_{xx}, V_{xx})$ and $m(0, V_{\text{oc}})$. Therefore, V_i, that is, V_1 to V_6, are obtained by taking the median of the voltage at the upper and lower bound coordinate. For example, the voltage at f is the median of V_{xxx} and V_{mpp}. That is $V_3 = (V_{xxx} + V_{\text{mpp}})/2$. Using the boundary coordinates of these 12 linear segments together with the measurement of the PVE current, the linear equation of every segment can be determined. This equation follows the form of the equation of a straight line given the gradient and the intercept; $V_{\text{pve}} = m_i I_{\text{pve}} + c_i$, such that m_i, c_i are the respective slope and intercept of the line segments.

Therefore, by segmenting the I-V curve into these respective pieces together with their current boundary coordinates, the reference voltage for the PVE is generated. As such if the actual PVE current falls between respective current boundaries, the corresponding reference voltage equation is easily computed for that segment using the notion

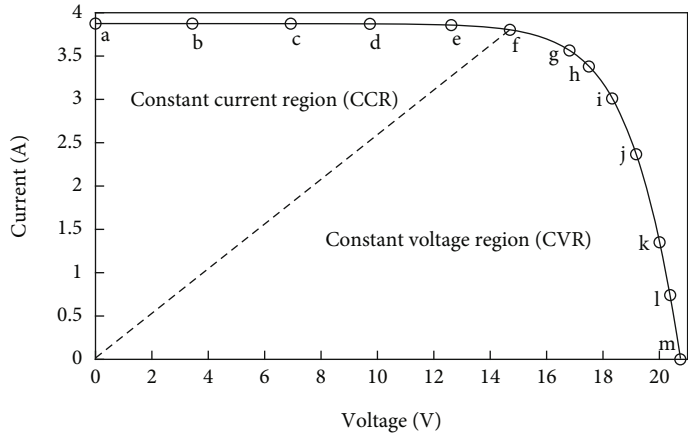

FIGURE 4: CCR/CVR recognition in the I-V curve: dotted lines separate the two regions.

of $V_{\text{pve}}(I_{\text{pve}}) = m_i I_{\text{pv}} + c_i$. The linear equations for the respective 12 segments are presented in Equations (A.7)–(A.17) of the appendix.

It is very important to distinguish two crucial regions of the I-V curve known as the constant current region (CCR) and constant voltage region (CVR) as shown in Figure 4. In the CCR, a small change in the current causes a large change in voltage, while a small change of the voltage in the CVR causes the current to escalate [7]. A major problem in the control of the power stage of the PVE lies in the fact that using a voltage controller, the reference voltage oscillates in the CCR, while using a current controller the reference current oscillates in the CVR. In this work, we consider a voltage controller; therefore, to alleviate the problem of oscillatory reference voltage in the CCR, a resistance feedback technique is employed. The resistance feedback strategy makes the proposed voltage controller behave as a pure voltage controller in the CVR and a current controller in the CCR, hence solving the problem of oscillations in the control of the PVE. As seen in Figure 4, we propose to recognize the boundary of the two regions using the dotted line in Figure 4. A close inspection of this figure shows that this boundary cut the $f(I_3, V_3)$ coordinate. Therefore, the CCR is the region from short-circuit (a) to $f(I_3, V_3)$, whose piecewise equations are defined as in Equations (A.7)–(A.11). Hence, once the CCR/CVR boundary is recognized, the CCR detected the load resistance information ($I_{\text{pv}} = V_{\text{pv}}/R$) fed into the general linear equation of the PVE, such that in the CCR, V_{pve} is computed as $V_{\text{pve}}(R) = c_i R/(R - m_i)$ for i running from 1 to 5. This principally means that we get rid of the current control problem in the CCR as $V_{\text{pv}}(R)$ is no longer a function of the current but the load resistance hence making the control effective. Therefore, Equations (A.7)–(A.11) of the appendix, provide a versatile and accurate voltage control scheme in the CCR. Conversely, when the CVR is detected, the voltage reference for the respective coordinates will be defined as in Equations (A.12)–(A.18) of the appendix. The proposed recognition is similar to a hybrid control stage, where a voltage controller is deployed in the CVR and a current controller in the CCR.

To ensure that the PVE operates over a broad spectrum, we propose to assist the linearization process using an artificial neural network (ANN). As such, we resort to training an ANN model which will predict the (voltage-current) boundary coordinates of the 12 respective segments.

In this work, an MSX-60W solar panel [22] was modeled and used to extract data to train the ANN. Using the setup in Figure 5, a data extraction algorithm was written to extract data from the PV model. For this training, we considered operating temperatures ranging from $10\circ$C to $50\circ$C, in steps of $2\circ$C with operating irradiance spanning from 100 W/m^2 to 1000 W/m^2 in steps of 50 W/m^2. The 12 segments with boundary coordinates (x, y) constitute 24 outputs for the ANN model.

The proposed linearization method was applied to the PV system under uniform irradiance conditions. The versatility of the proposed method makes it easily replicable for a PV system under partial shading conditions. A comprehensive flowchart algorithm for the proposed PVE is presented in Figure 6.

The ANN model structure is composed mainly of 2 neurons in the input layer, 10 hidden layer neurons, and 24 output neurons. Furthermore, the data ANN was trained using 70% of the dataset for training and 15%, respectively, for testing and validation. The input neurons are irradiance (G) and temperature (T), with the output being the 24 boundary coordinates of the 12 segments. The ANN structure was trained by Levenberg-Marquardt using the extracted data. The boundary coordinates available at the output of the ANN can then be utilized by the mathematical formulations in Equations (A.7)–(A.18), to supply a reference voltage to the PVE.

3.2. Power Conversion Stage and Nonlinear Controller. The power conversion stage (PCS) and nonlinear controller form the two other important subsystems of the proposed PVE. In this work, a nonlinear switch mode power supply based on the DC-DC buck converter is considered in the power stage. The full dynamics of the converter will then be exploited to design the nonlinear controller that should stabilize the PVE.

The buck has recently received attractive attention in the design of PVE [7, 12, 13]. The electrical circuit of a buck

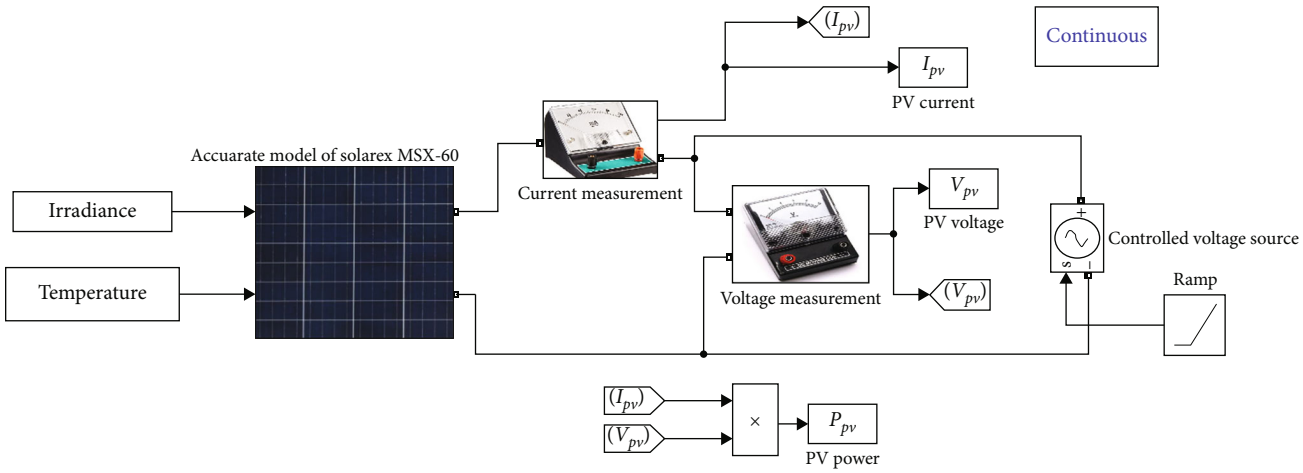

Figure 5: Data generation setup.

converter is shown in Figure 7. It consists of a transistor (k) controlled via a PWM control law, a diode (D), and two storage elements, the inductor (L) and capacitor; hence, the converter is a second-order system. The inductor carries current i_L. The DC load, in this case, modeled by a resistive element (R) carries the output current (I_{pve}), imposed by the PVE voltage V_{pve}. During the first mode of operation, the switch is on, and while the diode is blocked, the input voltage source (E) charges the storage elements and supplies energy to the load directly. In mode 2, the switch is off, and the diode comes on, ensuring the freewheeling of energy to the load. The parameters of the converters are chosen such it continuously operates the buck in continuous conduction mode, hence must satisfy the minimum criteria:

$$L_{\min} = \frac{(E - V_s)V_s}{\Delta I_L f_S E}. \tag{5}$$

A good estimate of the inductor ripple current (ΔI_L) is 20% to 40% of the output current. In Equation (5), the actual inductor must be greater than $L_{\min}$, that is, $L > L_{\min}$. Similarly, the capacitance follows a similar design based on the desired value of output voltage ripple, where $C > C_{\min}$.

$$C_{\min} = \frac{\Delta I_L}{8 f_s \Delta V_s}, \tag{6}$$

where ΔV_s is the desired output voltage ripple and f_s the switching frequency. To design a nonlinear controller for the converter, its full dynamics must be defined. Considering the averaged model of such a converter to be the following [23]:

$$\begin{cases} \dot{x}_1 = -\dfrac{1}{L}x_2 + u_{\text{pve}}\dfrac{E}{L}, \\ \dot{x}_2 = \dfrac{1}{C}x_1 - \dfrac{1}{RC}x_2, \end{cases} \tag{7}$$

where x_1, x_2 denote the average inductor current (i_L) and PVE voltage (V_{pve}), respectively. u_{pve} is the average value of the duty cycle. A nonlinear controller that stabilizes the PVE can then be designed to exploit the full dynamics of Equation (7).

Unlike numerous PVE works in the literature, where the control of the PVE is based on linear control, in this work, we present a pure nonlinear controller designed to exploit the full dynamics of the converter. The nonlinear controller is based on backstepping, which is a recursive methodology, involving a systematic construction of control laws and Lyapunov functions. In the nonlinear control design, we desire to force the PVE voltage x_2 to operate at the PVE reference $x_{\text{r.pve}}$. Therefore, the error resulting from the deviation of the PVE voltage from the reference $z_1 = x_2 - x_r$ must turn to zero, where $x_r = x_{\text{r.pve}}$. Defining the dynamics of this error by taking its first derivative with the use of Equation (7), it follows that

$$\dot{z_1} = \dot{x_2} - \dot{x_r} = \frac{1}{C}x_1 - \frac{1}{RC}x_2 - \dot{x_r}. \tag{8}$$

In Equation (8), x_1/C behaves as a virtual control input. Such an equation shows that one gets $\dot{z_1} = -c_1 z_1$ ($c_1 > 0$, being a design parameter) provided that

$$\frac{x_1}{C} = -c_1 z_1 + \frac{1}{RC}x_2 + \dot{x_r}. \tag{9}$$

Given that x_1/C is just a variable and not an effective control input, Equation (8) cannot be enforced for all $t \geq 0$. However, from Equation (9), we can define the desired value of x_1/C as

$$\alpha_1 = -c_1 z_1 \frac{1}{RC}x_2 + \dot{x_r}. \tag{10}$$

One defines the error between the desired and actual virtual input (z_2) as

$$z_2 = \frac{x_1}{C} - \alpha_1. \tag{11}$$

If z_2 decays asymptotically to zero, then the desired control goal stated as "z_1 turning to zero" is achieved. To this

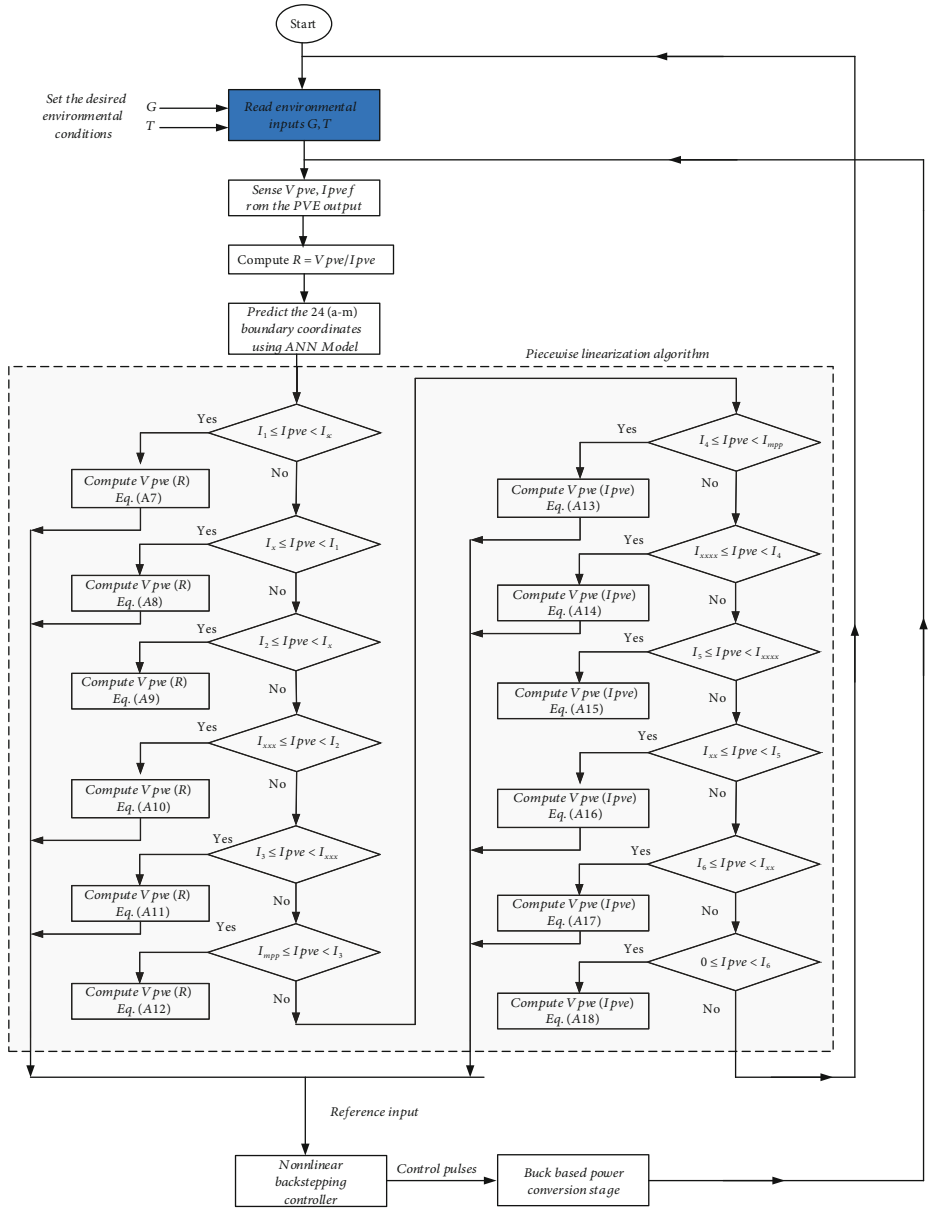

Figure 6: Comprehensive flowchart algorithm of the proposed photovoltaic emulator.

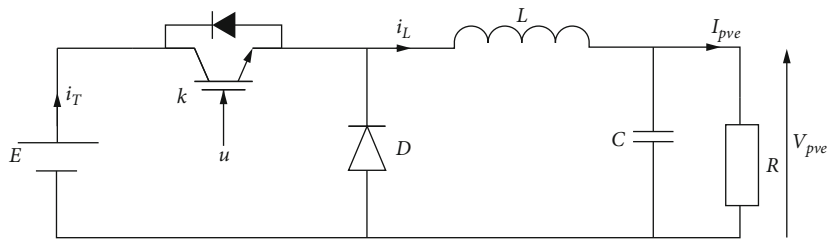

Figure 7: Buck converter electrical circuit.

end, the desired value of α_1 is called a stabilization function. Replacing x_1/C by $(z_2 + \alpha_1)$ gives $\dot{z_1} = z_2 + \alpha_1 - (1/RC)x_2 - \dot{x_r}$ which in conjunction with Equation (10) returns

$$\dot{z_1} = -c_1 z_1 + z_2. \tag{12}$$

Defining the time derivative of z_2, with Equations (7) and (11), in view of investigating its dynamics, we have that

$$\dot{z}_2 = \frac{\dot{x}_1}{C} - \dot{\alpha}_1 = -\frac{x_2}{LC} + u\frac{E}{LC} - \alpha_1. \tag{13}$$

From Equation (10), one has

$$\dot{\alpha}_1 = c_1^2 z_1 - c_1 z_2 + \frac{x_1}{RC^2} - \frac{x_2}{(RC)^2} + \ddot{x}_r. \tag{14}$$

Using Equations (14) and (13), we have

$$\dot{z}_2 = -c_1^2 z_1 + c_1 z_2 - \frac{x_1}{RC^2} + \left[\frac{1}{(RC)^2} - \frac{1}{LC}\right] x_2 + u\frac{E}{L} - \ddot{x}_r. \tag{15}$$

With the new error system (z_1, z_2), the controlled system of Equation (7) is expressed by a couple of Equations (12) and (15). It is therefore imperative to define a composite Lyapunov function that ensures that the error system (z_1, z_2) vanishes to zero that is $(z_1, z_2) = (0, 0)$. To this end, we define the composite Lyapunov $V_c = (1/2)z_1^2 + (1/2)z_2^2$. The dynamics of V_c via the time derivative along the (z_1, z_2) path is derived as

$$\dot{V}_c = z_1\dot{z}_1 + z_2\dot{z}_2 = -c_1 z_1^2 - c_2 z_2^2 + z_2(c_2 z_2 + z_1 + \dot{z}_2). \tag{16}$$

In Equation (16), c_2 is a design parameter, chosen such that $c_2 > 0$. It can be seen from Equation (16) that, if the term in brackets of z_2 that is $c_2 z_2 + z_1 + \dot{z}_2$ was zero, then the derivative of the Lyapunov function $\dot{V}_c$ would be negative which warrants the global asymptotically stability of the system in that case. Exploiting this possibility, by so doing one deduced that when $c_2 z_2 + z_1 + \dot{z}_2 = 0$, together with Equation (15), the following nonlinear control law is attained.

$$u_{\text{pve}} = \frac{LC}{E}\left[\left(c_1^2 - 1\right)z_1 - (c_1 + c_2)z_2 + \frac{x_1}{RC^2} - \left[\frac{1}{(RC)^2} - \frac{1}{LC}\right]x_2 + \ddot{x}_r\right]. \tag{17}$$

To this end, u_{pve} in Equation (17) is the nonlinear law that stabilizes the PVE power stage. As can be inferred from Equation (17), the controller which is an indispensable element of the PVE has two parameters, that is, c_1 and c_2. The performance of the controller is inherently dependent on these parameters. Consequently, the optimal design of the controller is supposed to ensure the optimal performance of the PVE.

3.3. Optimization of the PVE Using Particle Swarm Optimization. To ensure optimal performance of the PVE control stage, we propose to optimize it with particle swarm optimization. The theory of PSO is already well established in the literature and can be found [24, 25]. The dynamics of particles in the PSO swarm are represented by the equations:

$$\begin{aligned} x_{ij}^{n+1} &= x_{ij}^n + v_{ij}^{n+1}, \\ uv_{ij}^{n+1} &= \omega v_{ij}^n + r_1 A_1\left(p_{ij}^n - x_{ij}^n\right) + r_2 A_2\left(g_{ij}^n - x_{ij}^n\right), \end{aligned} \tag{18}$$

where $x_{ij}^{n+1}, v_{ij}^{n+1}$ are the position and velocity of particle i at $(n+1)$ iteration in j dimension. x_{ij}^n, v_{ij}^n are the position and velocity of particle i at (n) iteration in j dimension. ω is the inertia weight; A_1, A_2 are the self-weight and social acceleration coefficients, respectively. r_1 and r_2 are uniformly distributed random numbers between 0 and 1. p_{ij}^n is the best position of the best particle in j dimension evaluated at instant n, while g_{ij}^n is the global best position.

The inertial weight ω is defined as [24]

$$\omega = \omega_{\max} - \frac{\omega_{\max} - \omega_{\min}}{\text{iter}_{\max}} \times \text{iter}. \tag{19}$$

Once a problem has been identified as an optimization task, the next step is to formulate the optimization problem.

PSO is responsible to determine the optimal parameters of the PVE controller, c_1, c_2. In this light, the objective or cost function that permits the determination of optimal values of the parameters must be formulated. In the literature on control parameter optimization, numerous optimization cost functions can be spotted in the literature [26, 27] such as the integral of absolute error (IAE), integral square error (ISE), and integral of time squared error (ITSE). These cost functions exhibit exceptional performance in terms of error minimization. However, their main limitation lies in the fact that the steady-state error objective is usually satisfactory at the detriment of some other key time domain control objectives such as overshoots, rise time, and selling time. For example, the disadvantage of the IAE and ISE criteria is that their minimization can result in a response with a relatively small overshoot but a long settling time because the ISE performance criterion weights all errors equally independent of time [28]. Although the ITSE performance criterion can overcome the disadvantage of the ISE criterion, the derivation processes of the analytical formula are complex and time-consuming [28]. To address this problem, Ref. [24] proposed an objective function that harnesses the minimal error objective and the optimization of overshoots (M_p), rise time (t_r), and settling time (t_s) defined as

$$F(c)_{\min} = \alpha\left(M_p + \text{ISE}\right) + \beta(t_r + t_s), \tag{20}$$

where ISE is $\text{ISE} = \int_0^t z_1^2(t)$. Recalling that we desire to act on error z_1, between the actual PVE voltage and the desired reference. The objective in Equation (20) permits us to have control over the value of M_p, t_r, t_s with the weighing coefficients α and β. The most important parameter in this cost function is the ISE. Based on its definition, the parameter forces the other parameters to be optimum. Hence, to have a minimum ISE, the other parameters have to be in their minimum possible values. Therefore, minimizing the cost function $F(c)$ is directly related to the optimization of M_p, t_r, t_s in the cost function [24]. In addition to the optimization of M_p, t_r, t_s, we desire to also optimize the peak time of the PVE response (t_p). This permits us to modify the cost function of [24] to

$$F(c)_{\min} = \alpha\left(M_p + \text{ISE}\right) + \beta\left(t_r + t_s + t_p\right). \tag{21}$$

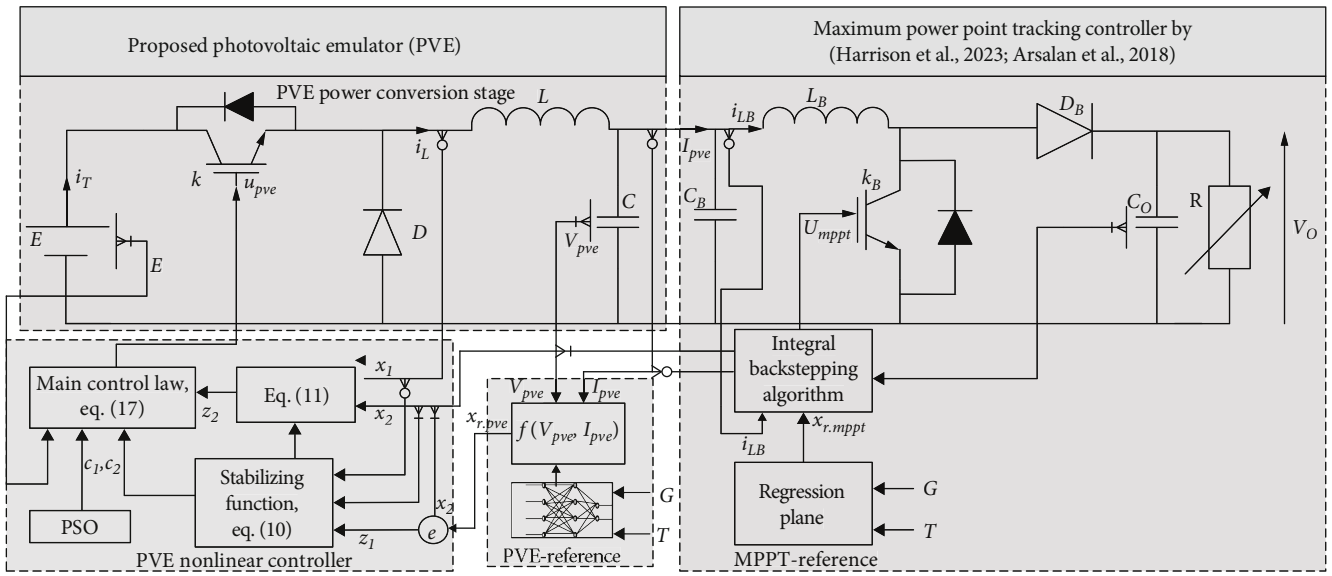

Figure 8: Architecture of the proposed PVE coupled with an MPPT controller (MPPT stage from [33, 34]).

To this end, Equation (21) represents the cost function proposed in this paper. It is a natural practice to optimize a controller for a step response of its input [29]. To optimize the PVE, the buck converter (power stage) and the controller are decoupled from the architecture system of Figure 8. This enables the power stage to be subjected to a step response in reference voltage at a fixed PVE resistance.

4. Application of the PVE for Simulating and Validation of MPPT Algorithms/Controllers

A PV system is subject to environmental conditions, including temperature and irradiance. The continuous variation of these conditions induces the systematic variation of the maximum power point (MPP). Therefore, it becomes imperative to continually track this point and ensure that PV systems operate at their maximum energy potential [20]. In the spirit of optimizing PV systems, numerous maximum power point tracking (MPPT) algorithms/controllers have been developed in this recent decade [19, 30–33]. The perturb and observe (P&O) and incremental conductance algorithm (INC) are the most popular MPPT algorithms/controllers. Although these algorithms are simple in terms of implementation, they present numerous problems such as the trade-off between accuracy and speed and oscillations under fast-changing operating conditions. Numerous attempts in the form of modifications and hybrid techniques have been proposed to improve the performance of these algorithms. However, according to [34], it would be more suitable to subject the PV system to a nonlinear MPPT control. This appears to be a promising strategy because the PV system is inherently nonlinear. To the best of our knowledge, the integral backstepping controller is one of the most performant MPPT techniques that has been recently applied to PV systems.

The works of [34] show that the integral backstepping controller is better than the P&O, INC, backstepping, and fuzzy logic MPPT controllers. Therefore, in this paper, we are going to resort to the integral backstepping MPPT controller to assess the proposed PV emulator.

The good number of articles we came across from the literature including [13–16] did not carry out in-depth MPPT assessment of their PVE. Therefore, the PVE proposed in this paper will offer a suitable platform for simulating and validating MPPT controllers.

The architecture of the PVE coupled with an MPPT controller is presented in Figure 8. It is made up of two stages, namely, the PVE and the maximum power point tracking (MPPT) controller. As seen from the figure, the PVE adopts its three main subsystems, the power conversion stage (PCS), the nonlinear controller, and the PVE reference. The second stage, as seen in Figure 8, is the maximum power point tracking controller. In the first stage, the power conversion stage is controlled by the PVE nonlinear controller. As seen in Figure 8, the controller is governed by the resolutions of Equations (10) and (11) and the main control law (17). Moreover, the main control law is supplied with the optimal parameters of the controller, c_1 and c_2, from the PSO algorithm. Hence, by feeding the controller with the PVE reference voltage, the buck converter in the power stage is optimally driven to operate at a stated reference. Furthermore, the MPPT controller in the second stage is composed of the dc-dc boost converter, coupled with a DC load (R) and an integral backstepping control algorithm. The reference for the MPPT system is provided by a constructed regression plane as proposed by Arsalan et al. [34]. Therefore, Figure 8 is a typical PV system where the PV source has been replaced by our proposed emulator. Furthermore, it is presented as the proposed architecture suitable for simulating and validating MPPT controllers. In this paper, we consider the nonlinear integral backstepping controller recently proposed by [34] to simulate and assess the proposed PVE. It is worth noting that [34] developed the integral backstepping algorithm for a noninverting buck-boost

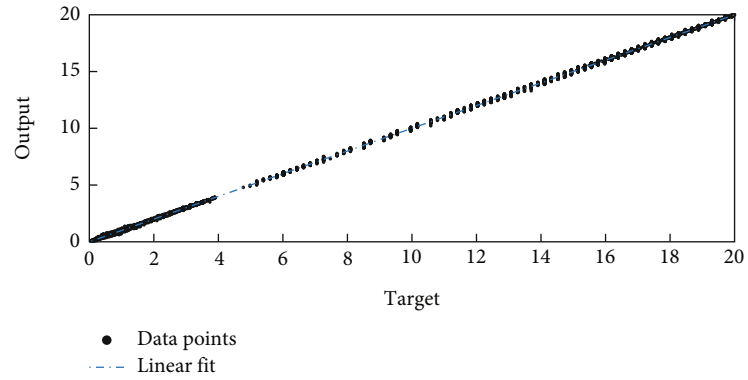

Figure 9: Regression plot of the ANN model for all the datasets (training, validation, and testing): regression coefficient = 0.99995 and mean square error (MSE) = 0.0057967.

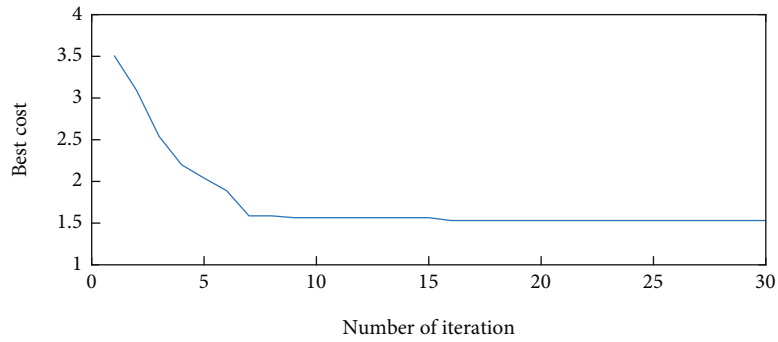

Figure 10: Optimal convergence of the PVE control system with the number of iterations.

converter. Therefore, in this paper, we refer to the control algorithm developed for a boost converter as seen in the recently published work of [33].

To ensure that the system operates at the maximum power point, Ref. [33] derived the following nonlinear control law (u_{mppt}):

$$u_{\text{mppt}} = 1 - \frac{L_B}{V_o}\left(K_2 e_2 + \frac{V_{\text{pve}}}{L_B} + K_1^2 C_B e_1 + K_1 e_2 + kK_1 C_B p - \dot{I}_{\text{pve}} + C_B \ddot{x}_{\text{r.mppt}} - C_B k e_1 - \frac{e_1}{C_B}\right), \tag{22}$$

where $e_1 = V_{\text{pve}} - \ddot{x}_{\text{r.mppt}}$, $\varphi = C_B(K_1 e_1 + (I_{\text{pve}}/C_B) - \dot{x}_{1\text{ref}} + k p)$, $e_2 = x_2 - \varphi$, and $p = \int_o^t (e_1) dt$.

As seen in Equation (17) and Figure 8, C_B and L_B are the capacitance and inductance of the boost converter in the MPPT controller, while K_1, K_2, and K are the parameters of the controller.

The configuration in Figure 8 is highly versatile; hence, other MPPT controllers can be simulated by direct coupling of the respective MPPT to the PVE.

5. Results and Discussions

In this paper, we proposed to replace PV modules with a high-performance emulator that can ensure a controllable testing environment suitable for testing PV systems. All the investigations presented in this paper are carried out in MATLAB/Simulink environment. The performance of the ANN model trained in this work is presented in Figure 9. It was found the regression coefficient and mean squared error of the model for all the dataset (70% training, 15% validation, and 15% testing). The good correlation coefficient between the target and the output data of the model and the very low MSE suggest the very high performance of the ANN model.

During the optimization of the PVE, we found that the best cost of the optimization obeyed the profile in Figure 10. The optimization was performed optimized for a step change in operating condition. To achieve this, we decoupled the MPPT from the whole system and provided a step change of 10 V to the controller. In addition, the PVE resistance at its terminal was maintained at 15 Ω during the optimization process.

It can be seen in Figure 10 that the system converged after 17 iterations. At the point of convergence, we extracted the optimal parameters of the controller c_1 and c_2. Their respective values are presented in Table 1.

5.1. Accuracy of the Proposed PVE. An accurate PVE is supposed to produce similar characteristics as the PV model over a broad spectrum of environmental conditions. Assessing the accuracy of the proposed PVE, we found that it

Table 1: Key parameters of the proposed PVE and the tested MPPT controller.

System parameters	Value
PVE input supply voltage (E)	22 V
PVE switching frequency (f_s)	31.37 kHz
PVE inductor (L)	5 mH
PVE capacitance (C)	30 μ F
PSO functional parameters $[A_1, A_2]$	[2, 2]
PVE-optimal control parameters $[c_1, c_2]$	$[8.05 \times 10^3, 5.23 \times 10^3]$
MPPT controller parameters $[K_1, K_2, K]$	[9000, 10000, 2045]
MPPT boost converter parameters $[C_B, L_B, C_o]$	[250 μF, 5 mH, 200 μF]

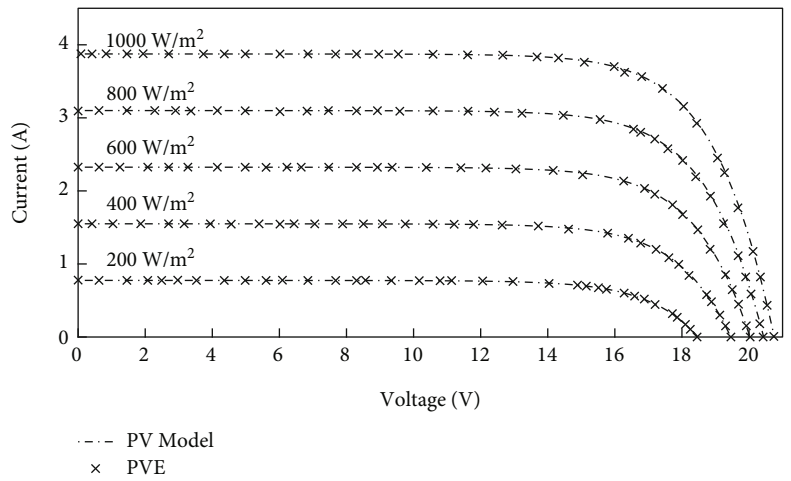

Figure 11: Emulated $(V_{\text{pve}} - I_{\text{pve}})$ points plotted on the PV model current-voltage characteristics.

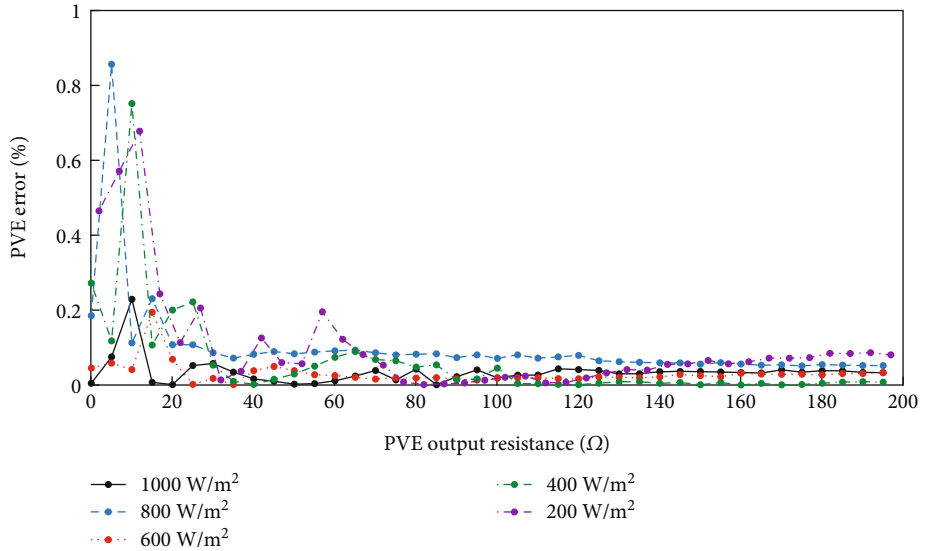

Figure 12: Accuracy of the PVE, measured by the relative error as a function of the output resistance for varying irradiance and constant temperature (25 ∘ C).

exhibited similar features as the PVE model as shown in Figure 11. The result was obtained by varying the PVE output resistance from the short circuit to the open circuit. It can be seen that the proposed PVE covers the entire I-V curve. By inspection, we see that the proposed PVE closely fits the I-V curve of the PV model. Furthermore, it can be seen that even during extreme control conditions (1000 W/mm^2 and 200 W/m^2), the proposed PVE still covered the entire I-V curve, hence suggesting that the proposed PVE can be used to conduct a short-circuit or open-circuit test. The operational range of the proposed PVE is better than that of [16], where the PVE is limited to a small range of the I-V curve and cannot run from the short circuit to the open circuit. The lower limit/range of operation is attributable to the small-scale control performance of the PI controller.

To allow a detailed view of the accuracy of the PVE, we computed its error for different operating conditions. The PVE error E_{pve} is mathematically written as

$$E_{\text{pve}} = \frac{V_{\text{pve}} - V_{\text{pv}}}{V_{\text{pv}}} \times 100, \tag{23}$$

where V_{pve} is the output voltage of the PVE and V_{pv} is the output voltage of the PV model under the same conditions.

The load at the output of the PVE was varied from 0.1 Ω to 200 Ω in steps of 5 Ω, hence allowing a good coverage of the I-V curve from short circuit to open circuit. The variation of the PVE error E_{pve} computed according to Equation (23), as a function of the output resistance, with irradiance running ranging from 200 W/m^2 to 1000 W/m^2, is shown in Figure 12. For the operating condition corresponding to 200 W/m^2, the closest resistance to the short-circuit point was noted to be 0.5 Ω; hence, the curve in Figure 12 begins at the output resistance of 0.5 Ω. For the other conditions, the output resistance was varied starting from 0.1 Ω. From the error distribution in Figure 13, we see that the maximum PVE error is lesser than 1% for irradiance ranging from 200 W/m^2 to 1000 W/m^2. The mean error of the PVE for these conditions was found less than 0.2% (see Table 2). By inspection of Figure 12, the greatest errors in the PVE were recorded at points closer to the maximum power point, for which the I-V curve demonstrated great nonlinearity. This is justified by the fact that the proposed PVE is based on linearization; therefore, regions of the I-V curve with higher nonlinear trends introduced high error due to linearization. This suggests that the accuracy of the PVE would increase if more linear segments were added around these inherent nonlinear regions of the I-V curve. The achieved accuracy of the proposed PVE is quite high and acceptable for a PV system. The 0.2% accuracy for operating conditions ranging from 200 W/m^2 to 1000 W/m^2 was found better than the 2.9% accuracy in [13]. We note that [13] resorted to complex analytical and numerical solutions to solve the nonlinear equations of the PV. The better accuracy achieved by this PVE could be an indication that the proposed linearization of the I-V curve is better than the direct nonlinear resolution of the I-V curve.

Environmentally, a PV responds to two key parameters, including irradiance and temperatures. To further assess the proposed PVE, we considered its accuracy for varying temperatures. To realize this experiment, the load resistance of the PVE was again varied from 0.1 Ω to 200 Ω in steps of 5 Ω.

It can be seen in Figure 13 that the maximum error of the PVE was found to occur at 10 ∘ C. Consequently, the overall mean error under this temperature was recorded to be 0.4881% (see Table 2), which is further better than the 2.9% in [13]. A temperature of 10 ∘ C is considered an extreme condition and will not often be considered in the testing profile for PV system applications. More interestingly, the mean error of the PVE was found very low at the temperature of 50 ∘ C (see Table 2). Furthermore, for varying temperatures and fixed irradiance, the PVE error was found to be lowest at 20 ∘ C and 30 ∘ C, respectively, which is the frequent temperature range for testing most MPPT. Finally, for varying temperatures and irradiance as seen in Table 2 (rows 11–13), the accuracy of the PVE was recorded to be less than 0.1%.

5.2. Dynamic Assessment of the PVE in response to Fast-Changing Environmental Conditions. In addition to steady-state accuracy, a PVE is supposed to exhibit a good dynamic response. That is, the controller in the PVE should fast stabilize the PVE at the reference operating point. This suggests that the controller is a key element of the PVE. To appreciate the dynamics of the proposed PVE, we subjected it to fast-changing environmental operating conditions as shown in Figure 14.

The PVE voltage and current responses are shown in Figures 15 and 16, respectively. It is worth noting that the PVE has an initial settling time of 2.5 ms which is better than the 10 ms in [15]. The proposed PVE further shows an interesting dynamic response during changing irradiance marked by a small settling time of 0.4 ms and zero oscillation, which is the case in Figure 15, as the temperature rises from 35 ∘ C to 55 ∘ C and irradiance at the value of 600 W/m^2. The good performance of the overall PVE is justified by the fact that the controller ensures that the emulator operates at the reference voltage, which can be attested in Figure 15. Consequently, the current response in Figure 16 shows a good dynamic response. We can also see that there is no steady-state error nor oscillation during the different responses to fast-changing irradiance and temperature. These attractive dynamic results suggest that the PVE will exhibit the same dynamic features as the PV module when replaced by the latter.

5.3. Dynamic Assessment of the PVE under the EN 50530 Irradiance Profile. To further comment on the dynamic performance of the PVE, we subjected it to the European EN 50530 test, which involves subjecting the PVE to sequences of fast/slow-changing irradiance. The EN 50530 irradiance profile is shown in Figure 17. In response to EN 50530, the obtained voltage and current response of the proposed PVE is presented in Figures 18 and 19, respectively. It can be seen that the PVE voltage exactly follows the reference voltage, both for fast- and slow-changing sequences of

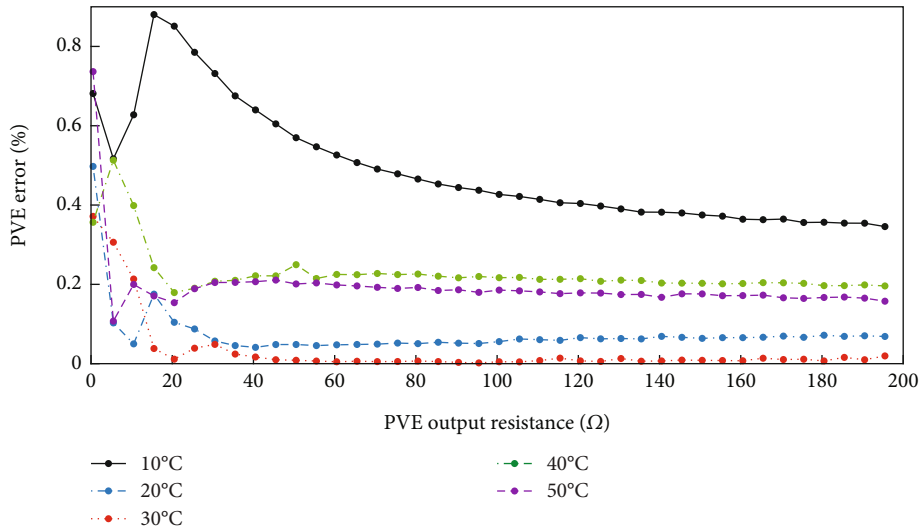

Figure 13: Accuracy of the PVE, measured by the relative error as a function of the output resistance for varying temperatures and constant irradiance ($1000\,W/m^2$).

Table 2: Mean error as a function of the PVE resistance (short circuit to open circuit).

No.	Irradiance (W/m^2)	Temperature (∘C)	Mean error (%)
1	1000	25	0.0342
2	800	25	0.0999
3	600	25	0.0305
4	400	25	0.0597
5	200	25	0.1022
6	1000	10	0.4881
7	1000	20	0.0753
8	1000	30	0.0331
9	1000	40	0.2276
10	1000	50	0.1941
11	700	38	0.0551
12	625	20	0.0757
13	430	39	0.0931

irradiance, with zero steady-state error. The result obtained so far demonstrates the excellent dynamic and robust performance of the PVE.

5.4. Dynamic Assessment of the PVE in response to Changing Load. In addition to varying environmental conditions, a PV panel is often connected to loads that are not fixed. Therefore, the PVE must exhibit the same features as the PV panel under changing load. That is, the PVE voltage increases following an increase in load resistance, which is associated with a drop in PVE current. More so, the voltage at the terminal of the PVE should decrease following a decrease in load resistance. To carry out this test, environmental conditions are held constant at standard test conditions (STC).

We found that when the load resistance decreased from $15\,\Omega$ to $8\,\Omega$, at the instant 0.1 s, the PVE voltage decreased from approximately 20 V to 19.14 V as inferred from Figure 20, consequently resulting in an increase in current from 1.35 A to 2.393 A as shown in Figure 21. We want to exalt the relatively small settling time of the PVE in response to the load decrease. This settling time was measured at 3 ms, faster than the 10 ms of [15]. In the emulator proposed by [15], the PI controller-based PVE showed significant oscillations due to changes in load. By visual inspection of Figures 20 and 21, one can attest that the PVE exhibit no oscillations. The supremacy of the nonlinear controller can further be appreciated by the fact that it ensures the excellent tracking of the reference voltage at zero steady-state error.

5.5. Dynamic Comparison of the Proposed PVE with a PI Controller-Based PVE. It is worth emphasizing that almost all the PVE available in the literature are based on the linear PI controller. In this subsection, we are going to compare the dynamic performance of the PI controller-based PVE with our nonlinear-based proposed PVE. The PI is a linear controller; hence, it demands that the system under control be linearized. To this end, a linearized model of the buck converter power stage as defined by [35] was obtained:

$$G_{\text{pcs}}(s) = \frac{\widehat{V}_{\text{pve}}(s)}{\widehat{d}(s)} = \frac{E/LC}{s^2 + s/RC + 1/LC}, \tag{24}$$

where $\widehat{V}_{\text{pve}}$ is the small signal of the PVE voltage (V_{pve}). The small signal of the duty cycle of the converter is denoted by $\widehat{d}$. Therefore, $G_{\text{pcs}}(s)$ is the linear control-to-output transfer function of the buck converter power conversion stage. On the other hand, the PI controller transfer function can be defined as

$$G_c(s) = \frac{\widehat{e}_{pi}(s)}{\widehat{d}(s)} = K_p + \frac{K_i}{s}, \tag{25}$$

where e_{pi} is the error between the reference and actual PVE voltage and $\widehat{e}_{pi}$ is the small signal of e_{pi}. The constants K_p

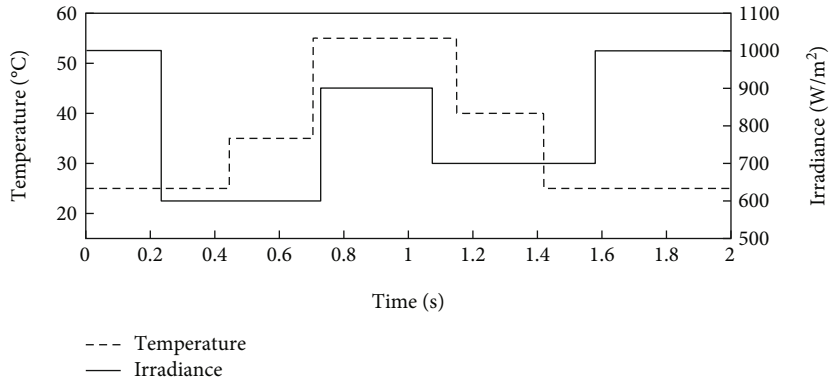

Figure 14: Fast-changing environmental conditions.

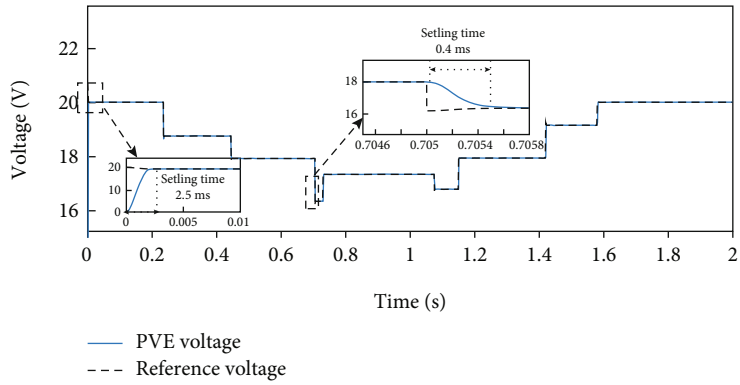

Figure 15: Response of the PVE to fast-changing irradiance (voltage).

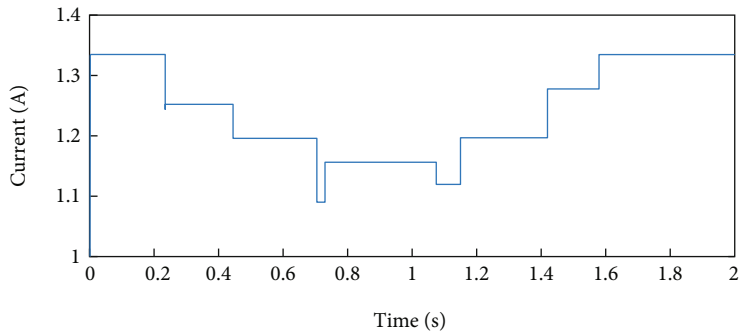

Figure 16: Response of the PVE to fast-changing irradiance (current).

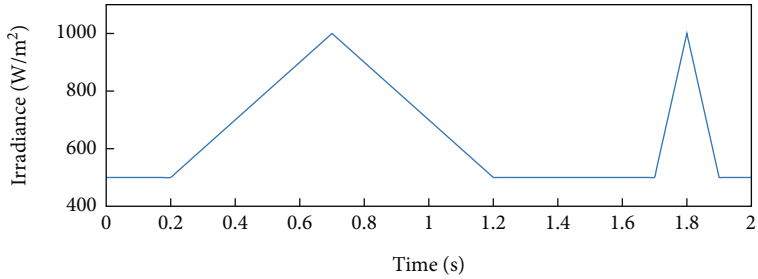

Figure 17: EN 50530 irradiance test profile.

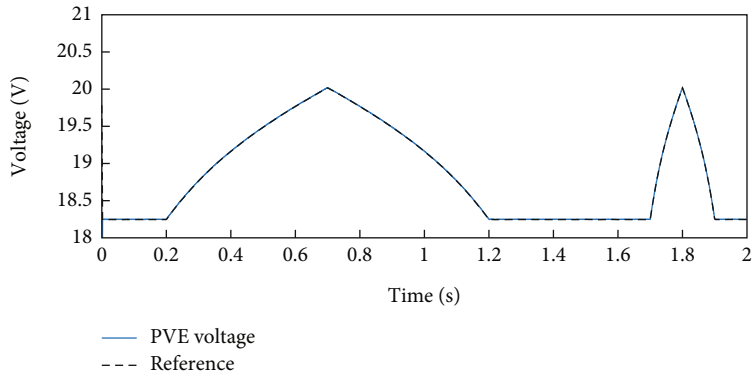

Figure 18: Response of the PVE to the EN 50530 irradiance (voltage).

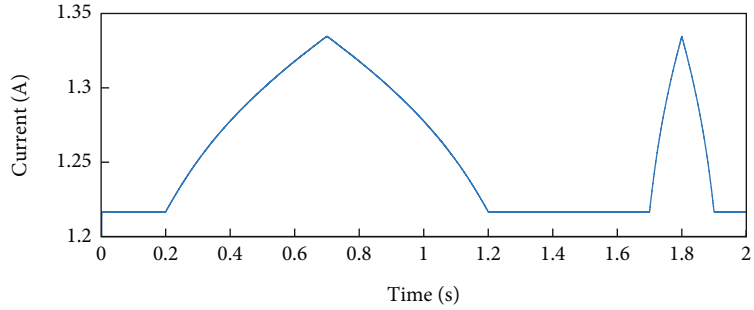

Figure 19: Response of the PVE to the EN 50530 irradiance (current).

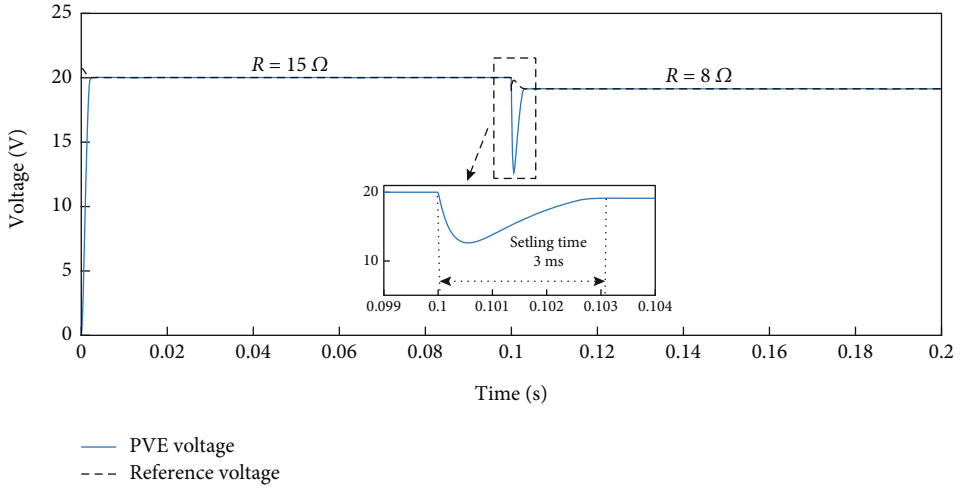

Figure 20: Response of the PVE to an abrupt change in load resistance (voltage).

and K_i are the parameters of the PI controller. These parameters were tuned using the "PI tunner" function in MATLAB/Simulink according to [36] for optimal dynamic response. The dynamic response of the PVE-PI controller and the proposed PVE nonlinear controller to fast-changing solar irradiance is shown in Figure 22. It can be seen that the proposed nonlinear controller converged faster than the PI controller at all the instances of changes in irradiance. When the irradiance increased to 1000 W/m^2, it was found that the settling time of the nonlinear and the PI controller was, respectively, 3 ms and 17 ms, which implies that the nonlinear controller is at least 5 times faster than the PI for this condition. A magnified view of the response for both controllers at 700 W/m^2 shows that the PI controller oscillates between approximately 19.2 V and 19.15 V around the reference voltage. This is an indication of the limited robustness of the PI controller. Conversely, the proposed nonlinear controller maintains the PVE voltage at the reference, with no oscillation nor steady-state error. This permits us to note that the proposed nonlinear controller has better dynamic and robust performances than the linear-based PI controller.

Furthermore, by subjecting the two PVEs with their respective controllers, to changing load, one can conclude their dynamic performances. The response of the two

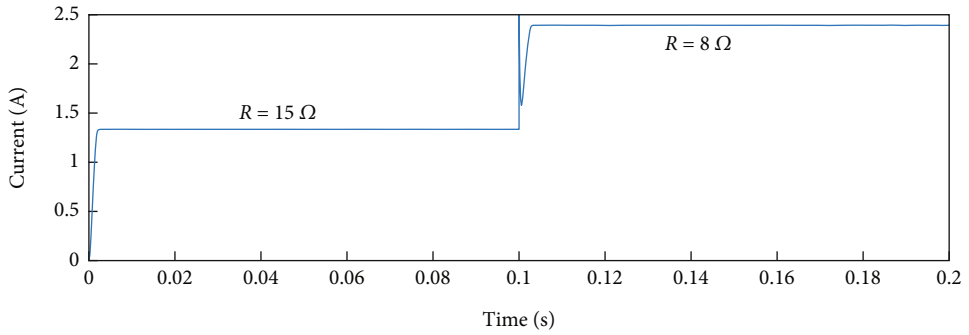

Figure 21: Response of the PVE to an abrupt change in load resistance (current).

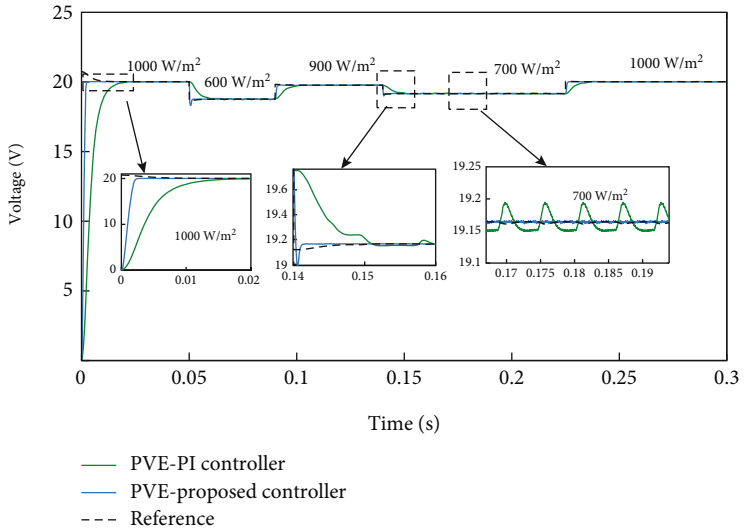

Figure 22: Dynamic performance comparison of the PVE-PI controller, with the proposed PVE nonlinear controller under changing irradiance.

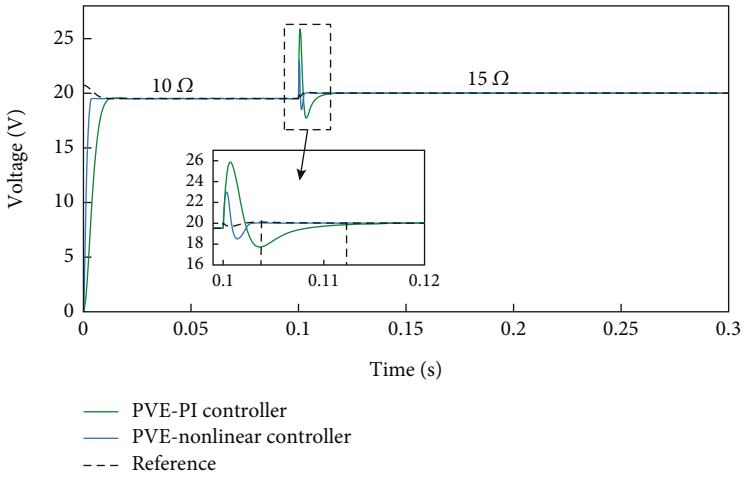

Figure 23: Dynamic performance comparison of the PVE-PI controller with the proposed PVE nonlinear controller under changing load.

controllers, to the change in load from 10 Ω to 15 Ω, is shown in Figure 23. It can further be confirmed that the proposed nonlinear controller is faster than the PI. In response to the change of load at 0.1 s, the PI controller exhibited relatively larger overshoots than the nonlinear controller. Moreover, the voltage response of the PI settled at 12.5 ms, as compared to the 3 ms of the nonlinear controller. This result, therefore, suggests that the proposed nonlinear controller is dynamically superior to the linear PI control.

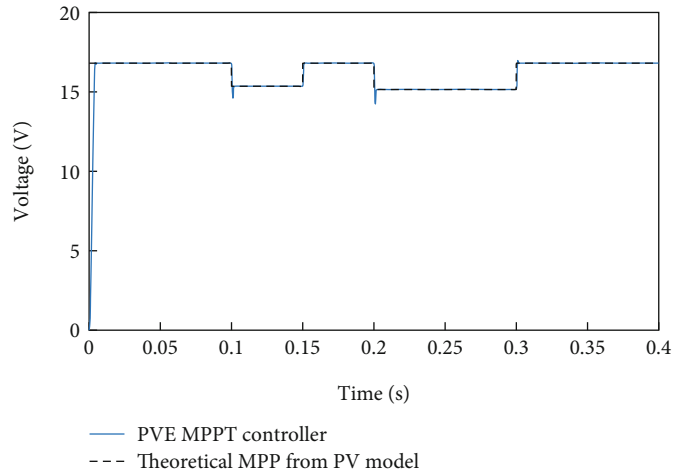

Figure 24: Voltage of the PVE system with MPPT control under fast-changing environmental conditions.

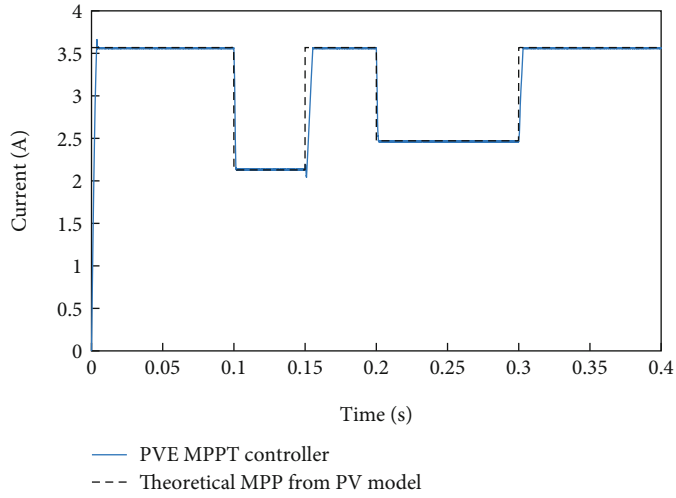

Figure 25: Current of the PVE system with MPPT control under fast-changing environmental conditions.

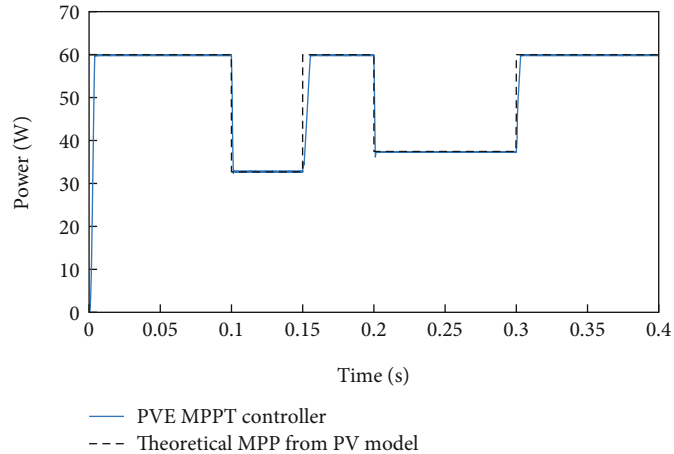

Figure 26: Power of the PVE system with MPPT control under fast-changing environmental conditions.

5.6. Application of the Proposed PVE for the Testing of the MPPT Controller. We are proposing a PVE suitable for simulating MPP controllers. In this light, the PVE was coupled to the nonlinear MPPT controller and two major tests were performed including the response to fast-changing irradiance and temperatures and the EN 50530 assessment.

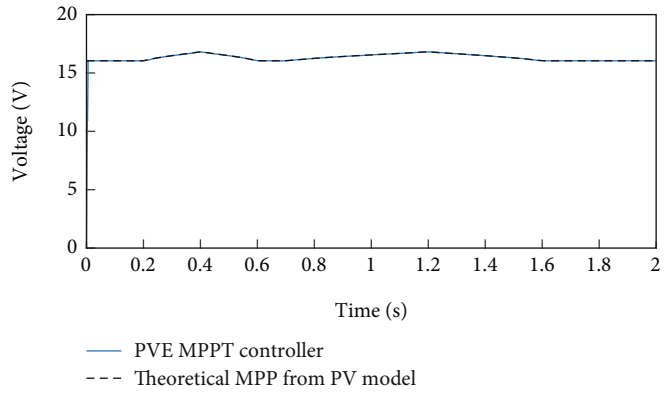

Figure 27: Voltage of the PVE system with MPPT control under the EN 50530 test.

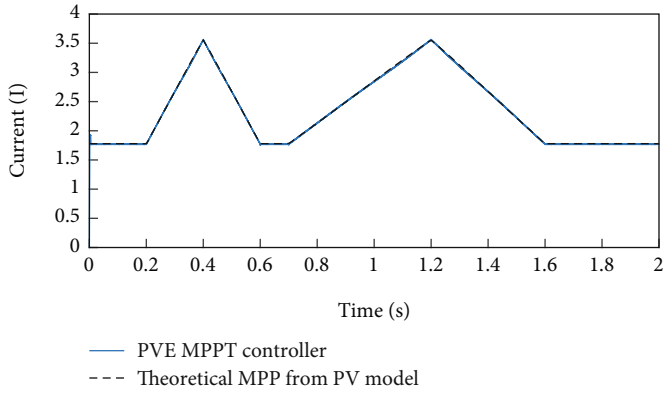

Figure 28: Current of the PVE system with MPPT control under the EN 50530 test.

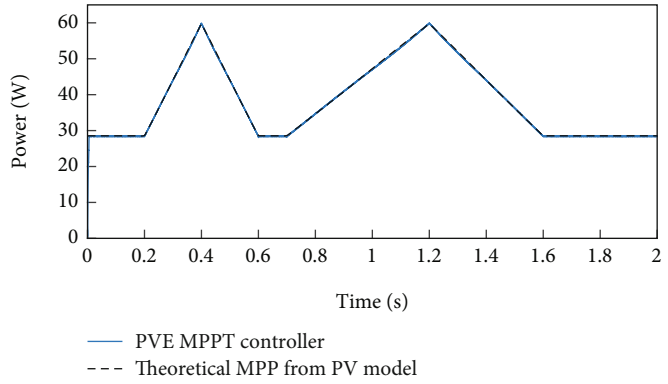

Figure 29: Power of the PVE system with MPPT control under the EN 50530 test.

During each of these tests, we computed the efficiency of the proposed PVE applied to the MPP controller.

5.6.1. PVE Coupled to MPPT Controller under Fast-Changing Irradiance and Temperatures. By subjecting the proposed PVE-MPPT controller to fast-changing irradiance and temperatures, we recorded the following response of the system. The voltage, current, and power of the PVE obtained during this test are shown in Figures 24–26, respectively.

To assess the proposed PVE, it was compared with the reference PVE model. In that light, Figures 24–26 also contain the theoretical MPP values of voltage, current, and power. These plots were directly obtained from the PV reference model. Therefore, by comparing the PVE power tracked by the MPP controller, with this theoretical power, we can quantify the efficiency of the proposed PVE in an MPPT context.

By inspection of Figures 24–26, we first appreciate that the MPPT controller is effective, as it effectively followed the theoretical MPP power. Also, the tracked power by the MPPT controller from the PVE is in close agreement with the theoretical MPP power from the PV model. By taking the ratio of the power under the PVE-MPPT controller to

that under the theoretical MPP, we get the efficiency of the PVE, written mathematically as

$$\eta_{\text{pve}} = \frac{\int_0^T P_{\text{pve-mppt}}}{\int_0^T P_{\text{theo.mpp}}}, \tag{26}$$

where $P_{\text{theo.mpp}}$ is the theoretical MPP obtained from the PV model and $P_{\text{pve-mppt}}$ the power of the tracked by the MPPT controller from the PVE.

By applying Equation (26), the efficiency of the PVE was computed and found to be 99.61% for fast-changing operating conditions.

5.6.2. PVE Coupled to MPPT Controller under the EN 50530 Test. To further comment on the efficiency of the proposed PVE and validate its suitability for simulating and testing MPPT controllers, the *EN 50530 test* was exhibited. The voltage, current, and power of the PVE system in response to the EN 50530 test can be seen in Figures 27–29. The effectiveness of the MPPT controller in tracking the MPP is worth praising. The MPPT controller effectively tracked the theoretical MPP voltage, current, and power as seen in the figures. This further suggests the high accuracy of the proposed PVE. Using Equation (26), the efficiency of the PVE was computed and found to be 99.5618%, which is quite high and attractive for a PV system.

The very high efficiency of the proposed PVE (>99.5%) suggests that the proposed PVE can replace the actual PV panel to ensure a realistic testing environment for MPT controllers.

6. Conclusion

A new high-performance photovoltaic emulator (PVE) was introduced in this paper. The PVE was proposed to replace solar panels and to provide a controllable and realistic environment suitable for testing PV systems, especially the maximum power point tracking (MPPT) controllers. The proposed PVE was constructed based on three main subsystems. A reference voltage generator, the power conversion stage (PCS), and the nonlinear control stage. To generate the accurate reference voltage for the PVE, we presented a new and fast resolution method for the *I-V* curve. The *I-V* curve was segmented into 12 linear pieces with assistance from a trained artificial neural network (ANN). By using the current-voltage coordinate of the linear segments, a reference voltage was generated for the PVE. This reference was used in the control stage to stabilize the PCS. The controller in the control stage was constructed based on the robust backstepping technology while its optimal performance was ensured by resorting to particle swarm optimization. The attractive features of the buck converter were employed in the power stage to ensure the effective transfer of energy from the PVE input to the output. By coupling the proposed PVE to a nonlinear-based MPPT controller, it was shown that the PVE offers high performance. Numerous tests including EN 50530 proved that the efficiency of the PVE is greater than 99.5%. Hence, the proposed PVE is very suitable for testing MPPT algorithms. The promising results achieved by this PVE are paving the way for the practical testing of numerous PV systems including MPPT controllers. In that light, the authors are tremendously working to release the full experimental prototype of this new PVE.

Appendix

A. Voltage Coordinates and Linear Equations of the PVE

The voltage coordinates and linear equations for the respective segments are presented as follows:

$$\begin{cases} V_x = \dfrac{V_{\text{oc}}}{2.44}, \\ V_{xx} = \dfrac{V_{\text{oc}} + V_{\text{mpp}}}{1.88}, \end{cases} \tag{A.1}$$

$$\begin{cases} V_{xxx} = \dfrac{V_x + V_{\text{mpp}}}{1.88}, \\ V_{xxxx} = \dfrac{V_{xx} + V_{\text{mpp}}}{2.44}, \end{cases} \tag{A.2}$$

$$V_1 = \frac{V_x}{2}, \tag{A.3}$$

$$V_6 = \frac{V_{xx} + V_{\text{oc}}}{2}, \tag{A.4}$$

$$\begin{cases} V_2 = \dfrac{V_x + V_{xxx}}{2}, \\ V_5 = \dfrac{V_{xxxx} + V_{xx}}{2}, \end{cases} \tag{A.5}$$

$$\begin{cases} V_3 = \dfrac{V_{\text{mpp}} + V_{xxx}}{2}, \\ V_4 = \dfrac{V_{\text{mp}} + V_{xxxx}}{2}, \end{cases} \tag{A.6}$$

$$\begin{aligned} V_{\text{pve}}(R) &= \frac{c_1 R}{R - m_1}\,;\, m_1 = \frac{V_1}{I_1 - I_{\text{sc}}}\,;\, c_1 \\ &= -m_1 I_{\text{sc}}\,;\, I_{\text{pv}} \in [I_1, I_{\text{sc}}], \end{aligned} \tag{A.7}$$

$$\begin{aligned} V_{\text{pve}}(R) &= \frac{c_2 R}{R - m_2}\,;\, m_2 = \frac{V_x - V_1}{I_x - I_1}\,;\, c_2 \\ &= V_x - m_2 I_x\,;\, I_{\text{pv}} \in [I_x, I_1], \end{aligned} \tag{A.8}$$

$$\begin{aligned} V_{\text{pve}}(R) &= \frac{c_3 R}{R - m_3}\,;\, m_3 = \frac{V_2 - V_x}{I_2 - I_x}\,;\, c_3 \\ &= V_x - m_3 I_x\,;\, I_{\text{pv}} \in [I_2, I_x], \end{aligned} \tag{A.9}$$

$$\begin{aligned} V_{\text{pve}}(R) &= \frac{c_4 R}{R - m_4}\,;\, m_4 = \frac{V_{xxx} - V_2}{I_{xxx} - I_2}\,;\, c_4 \\ &= V_{xxx} - m_4 I_{xxx}\,;\, I_{\text{pv}} \in [I_{xxx}, I_2], \end{aligned} \tag{A.10}$$

$$V_{\text{pve}}(R) = \frac{c_5 R}{R - m_5}\,;\, m_5 = \frac{V_3 - V_{xxx}}{I_3 - I_{xxx}}\,;\, c_5 = V_{xxx} - m_3 I_{xxx}\,;\, I_{\text{pv}} \in [I_3, I_{xxx}], \tag{A.11}$$

$$V_{\text{pve}}\left(I_{\text{pve}}\right) = m_6 I_{\text{pv}} + c_6\,;\, m_6 = \frac{V_{\text{mpp}} - V_3}{I_{\text{mpp}} - I_3}\,;\, c_6 = V_{\text{mpp}} - m_6 I_{\text{mpp}}\,;\, I_{\text{pv}} \in \left[I_{\text{mpp}}, I_3\right], \tag{A.12}$$

$$V_{\text{pve}}\left(I_{\text{pve}}\right) = m_7 I_{\text{pv}} + c_7\,;\, m_7 = \frac{V_4 - V_{\text{mpp}}}{I_4 - I_{\text{mpp}}}\,;\, c_7 = V_{\text{mpp}} - m_3 I_{\text{mpp}}\,;\, I_{\text{pv}} \in \left[I_4, I_{\text{mpp}}\right], \tag{A.13}$$

$$V_{\text{pve}}\left(I_{\text{pve}}\right) = m_8 I_{\text{pv}} + c_8\,;\, m_8 = \frac{V_{xxxx} - V_4}{I_{xxxx} - I_4}\,;\, c_8 = V_{xxxx} - m_8 I_{xxxx}\,;\, I_{\text{pv}} \in [I_{xxxx}, I_4], \tag{A.14}$$

$$V_{\text{pve}}\left(I_{\text{pve}}\right) = m_9 I_{pv} + c_9\,;\, m_9 = \frac{V_5 - V_{xxxx}}{I_5 - I_{xxxx}}\,;\, c_9 = V_{xxxx} - m_9 I_{xxxx}\,;\, I_{pv} \in [I_5, I_{xxxx}], \tag{A.15}$$

$$V_{\text{pve}}\left(I_{\text{pve}}\right) = m_{10} I_{\text{pv}} + c_{10}\,;\, m_{10} = \frac{V_{xx} - V_5}{I_{xx} - I_5}\,;\, c_{10} = V_{xx} - m_{10} I_{xx}\,;\, I_{\text{pv}} \in [I_{xx}, I_5], \tag{A.16}$$

$$V_{\text{pve}}\left(I_{\text{pve}}\right) = m_{11} I_{pv} + c_{11}\,;\, m_{11} = \frac{V_6 - V_{xx}}{I_6 - I_{xx}}\,;\, c_{11} = V_{xx} - m_{11} I_{xx}\,;\, I_{pv} \in [I_6, I_{xx}], \tag{A.17}$$

$$V_{\text{pv}}\left(I_{\text{pve}}\right) = m_{12} I_{\text{pv}} + c_{12}\,;\, m_{12} = \frac{V_6 - V_{\text{oc}}}{I_6}\,;\, c_3 = V_{\text{oc}}\,;\, I_{\text{pv}} \in [0, I_6]. \tag{A.18}$$

Data Availability

The data which supported the findings of this study are openly available in "figshare" at doi:10.6084/m9.figshare.21677555.v1 [37]. Also, the MATLAB/Simulink package for the proposed PVE is available with the corresponding author upon request.

Additional Points

Highlights. (1) Fast computation and resolution of the PV nonlinear equations by a new 12-segment-based linearization method. (2) Reference voltage generation assisted by artificial neural networks. (3) Photovoltaic emulator efficiency greater than 99.5% and accuracy less than 0.5%. (4) New nonlinear control of the photovoltaic emulator power conversion stage. (5) Optimization of the emulator using particle swarm optimization. (6) Coupling of the photovoltaic emulator with a recent nonlinear MPPT controller.

Conflicts of Interest

The authors declare that they have no conflicts of interest.

References

[1] Z. Dalala, M. Al-Omari, M. Al-Addous, M. Bdour, Y. Al-Khasawneh, and M. Alkasrawi, "Increased renewable energy penetration in national electrical grids constraints and solutions," *Energy*, vol. 246, article 123361, 2022.

[2] N. Hamsic, A. Schmelter, A. Mohd et al., "Increasing renewable energy penetration in isolated grids using a flywheel energy storage system," in *2007 International Conference on Power Engineering, Energy and Electrical Drives*, Setubal, Portugal, 2007.

[3] N. A. Matchanov, K. O. Seok, A. A. Mirzaev, M. A. Malikov, and D. S. Saidov, "Study of energy yield on grid connected micro-inverter type 2.24 kW PV system using PVsyst simulation software," *Applied Solar Energy*, vol. 56, no. 4, pp. 263–269, 2020.

[4] S. K. Sharma, D. K. Palwalia, and V. Shrivastava, "Performance analysis of grid-connected 10.6 kW (commercial) solar PV power generation system," *Applied Solar Energy*, vol. 55, no. 5, pp. 269–281, 2019.

[5] Y. Li, Z. Yang, G. Li, D. Zhao, and W. Tian, "Optimal scheduling of an isolated microgrid with battery storage considering load and renewable generation uncertainties," *IEEE Transactions on Industrial Electronics*, vol. 66, no. 2, pp. 1565–1575, 2019.

[6] T. Strasser, F. Andren, J. Kathan et al., "A review of architectures and concepts for intelligence in future electric energy systems," *IEEE Transactions on Industrial Electronics*, vol. 62, no. 4, pp. 2424–2438, 2015.

[7] I. D. G. Jayawardana, C. N. M. Ho, M. Pokharel, and G. E. Valderrama, "A fast-dynamic control scheme for a power-electronics-based PV emulator," *IEEE Journal of Photovoltaics*, vol. 11, no. 2, pp. 485–495, 2021.

[8] A. Koran, T. LaBella, and J.-S. Lai, "High efficiency photovoltaic source simulator with fast response time for solar power conditioning systems evaluation," *IEEE Transactions on Power Electronics*, vol. 29, no. 3, pp. 1285–1297, 2014.

[9] H. Nagayoshi, "I–V curve simulation by multi-module simulator using I–V magnifier circuit," *Solar Energy Materials and Solar Cells*, vol. 82, no. 1–2, pp. 159–167, 2004.

[10] S. Jin, D. Zhang, Z. Bao, and X. Liu, "High dynamic performance solar array simulator based on a SiC MOSFET linear power stage," *IEEE Transactions on Power Electronics*, vol. 33, no. 2, pp. 1682–1695, 2018.

[11] F. Yusivar, M. Y. Farabi, R. Suryadiningrat, W. W. Ananduta, and Y. Syaifudin, "Buck-converter photovoltaic simulator," *International Journal of Power Electronics and Drive Systems (IJPEDS)*, vol. 1, no. 2, pp. 156–167, 2011.

[12] T. Sudhakar Babu, S. Mohammed Azharuddin, B. Nishant, and N. Rajasekar, "A dynamic photo voltaic emulator using dSPACE controller with high accuracy solar photo voltaic characteristics," *Journal of Renewable and Sustainable Energy*, vol. 8, no. 1, article 015503, 2016.

[13] I. Moussa and A. Khedher, "Photovoltaic emulator based on PV simulator RT implementation using XSG tools for an FPGA control: theory and experimentation," *International Transactions on Electrical Energy Systems*, vol. 29, no. 8, 2019.

[14] Y. Mallal, L. El Bahir, and T. Hassboun, "High-performance emulator for fixed photovoltaic panels," *International Journal of Photoenergy*, vol. 2019, Article ID 3951841, 11 pages, 2019.

[15] K. T. Saraswathi, P. Arumugam, G. V. Swaminathan, and S. Periasamy, "An artificial neural network-based

comprehensive solar photovoltaic emulator," *International Journal of Photoenergy*, vol. 2022, Article ID 4741428, 14 pages, 2022.

[16] R. Ayop and C. W. Tan, "Rapid prototyping of photovoltaic emulator using buck converter based on fast convergence resistance feedback method," *IEEE Transactions on Power Electronics*, vol. 34, no. 9, pp. 8715–8723, 2019.

[17] S. Senthilkumar, V. Mohan, S. P. Mangaiyarkarasi, and M. Karthikeyan, "Analysis of single-diode PV model and optimized MPPT model for different environmental conditions," *International Transactions on Electrical Energy Systems*, vol. 2022, article 4980843, 17 pages, 2022.

[18] H. Bellia, R. Youcef, and M. Fatima, "A detailed modeling of photovoltaic module using MATLAB," *NRIAG Journal of Astronomy and Geophysics*, vol. 3, no. 1, pp. 53–61, 2014.

[19] A. Harrison, E. M. Nfah, J. de Dieu Nguimfack Ndongmo, and N. H. Alombah, "An enhanced P&O MPPT algorithm for PV systems with fast dynamic and steady-state response under real irradiance and temperature conditions," *International Journal of Photoenergy*, vol. 2022, Article ID 6009632, 21 pages, 2022.

[20] A. Harrison, J. de Dieu Nguimfack Ndongmo, and N. H. Alombah, "Robust nonlinear control and maximum power point tracking in PV solar energy system under real environmental conditions," *Engineering Proceedings*, vol. 31, no. 1, p. 49, 2023.

[21] J. A. Kratochvil, W. E. Boyson, and D. L. King, "Photovoltaic array performance model," August 2004, http://www.osti.gov, https://www.osti.gov/servlets/purl/919131.

[22] Solarex, *Solarex MSX-60 (Solar Module) PDF | PDF | Photovoltaics | Solar Panel*, Scribd, 2022, https://it.scribd.com/document/379381031/Solarex-MSX-60-solar-module-pdf.

[23] R. D. Middlebrook and S. Cuk, "A general unified approach to modelling switching-converter power stages," in *1976 IEEE Power Electronics Specialists Conference*, Cleveland, OH, USA, 1976.

[24] M. Rahimian and K. Raahemifar, "Optimal PID controller design for AVR system using particle swarm optimization algorithm," in *2011 24th Canadian Conference on Electrical and Computer Engineering(CCECE)*, Niagara Falls, ON, Canada, May 2011.

[25] F. M. Oliveira, S. A. O. da Silva, F. R. Durand, and L. P. Sampaio, "Application of PSO method for maximum power point extraction in photovoltaic systems under partial shading conditions," in *2015 IEEE 13th Brazilian Power Electronics Conference and 1st Southern Power Electronics Conference (COBEP/SPEC)*, Fortaleza, Brazil, November 2015http://ieeexplore.ieee.org/document/7420175/.

[26] R. A. Krohling and J. P. Rey, "Design of optimal disturbance rejection PID controllers using genetic algorithms," *IEEE Transactions on Evolutionary Computation*, vol. 5, no. 1, pp. 78–82, 2001.

[27] A. Saxena, Y. M. Dubey, and M. Kumar, "PSO and fuzzy based tuning mechanism for optimization of transient response in high-performance drilling machine," in *2020 7th International Conference on Signal Processing and Integrated Networks (SPIN)*, Noida, India, 2020https://ieeexplore.ieee.org/document/9071215.

[28] M. Nasri, H. Nezamabadi-pour, and M. Maghfoori, "A PSO-based optimum design of PID controller for a linear brushless DC motor," *World Academy of Science, Engineering and Technology*, vol. 1, no. 40, pp. 171–175, 2007, https://www.semanticscholar.org/paper/A-PSO-Based-Optimum-Design-of-PID-Controller-for-a-Nasri-Nezamabadi-pour/b4bb1a62d529dd8a6e227413172207c3c977f53b.

[29] F. Yacef, O. Bouhali, M. Hamerlain, and A. Rezoug, "PSO optimization of integral backstepping controller for quadrotor attitude stabilization," in *3rd International Conference on Systems and Control*, Algiers, Algeria, October 2013.

[30] T. Esram and P. L. Chapman, "Comparison of photovoltaic array maximum power point tracking techniques," *IEEE Transactions on Energy Conversion*, vol. 22, no. 2, pp. 439–449, 2007.

[31] J. Ahmed and Z. Salam, "A critical evaluation on maximum power point tracking methods for partial shading in PV systems," *Renewable and Sustainable Energy Reviews*, vol. 47, pp. 933–953, 2015.

[32] A. Gupta, Y. K. Chauhan, and R. K. Pachauri, "A comparative investigation of maximum power point tracking methods for solar PV system," *Solar Energy*, vol. 136, pp. 236–253, 2016.

[33] A. Harrison, N. H. Alombah, and J. de Dieu Nguimfack Ndongmo, "A new hybrid MPPT based on incremental conductance-integral backstepping controller applied to a PV system under fast-changing operating conditions," *International Journal of Photoenergy*, vol. 2023, Article ID 9931481, 17 pages, 2023.

[34] M. Arsalan, R. Iftikhar, I. Ahmad, A. Hasan, K. Sabahat, and A. Javeria, "MPPT for photovoltaic system using nonlinear backstepping controller with integral action," *Solar Energy*, vol. 170, pp. 192–200, 2018.

[35] B. Hekimoglu and S. Ekinci, "Optimally designed PID controller for a DC-DC buck converter via a hybrid whale optimization algorithm with simulated annealing," *Electrica*, vol. 20, no. 1, pp. 19–27, 2020.

[36] R. Ayop, C. Wei Tan, and A. Lawan Bukar, "Simple and fast computation photovoltaic emulator using shift controller," *IET Renewable Power Generation*, vol. 14, no. 11, pp. 2017–2026, 2020.

[37] A. Harrison and N. Henry Alombah, *Solar PV data: (a-m) piecewise segmentation of the I-V curve*, figshare, 2022.